Fabrication of La-Doped MoS$_2$ Nanosheets with Tuned Bandgap for Dye Degradation and Antimicrobial Activities, Experimental and Computational Investigations

Muhammad Ikram,* Binas Ilyas, Ali Haider, Junaid Haider, Anwar Ul-Hamid, Anum Shahzadi, Souraya Goumri-Said, Mohammed Benali Kanoun, Walid Nabgan,* and Asif Mahmood*

The development of efficient catalysts with a large number of active sites, tunable bandgap, and large surface area has been very challenging. In addition, a significant bottleneck in the application of catalysts for water treatment is their dissolution under extreme conditions, such as highly acidic or highly alkaline conditions that lead to poor application of the reported materials in real-world applications. In this study, the lanthanum (La)-doped molybdenum disulfide (MoS$_2$) nanosheets are reported for efficient breakdown of toxic pollutants from wastewater under a wide pH range from strongly alkaline to strongly acidic solutions. The La-MoS$_2$ nanosheets (NSs) are prepared by a facile hydrothermal approach using a two-step methodology. A redshift is observed upon La doping, indicating that the bandgap is lowered after La doping in MoS$_2$. The changes in bandgap and electronic structure are further investigated using the density functional theory (DFT), which reveal that doping of La introduces new states within the bandgap region, allowing for further induced energy transitions. The La-MoS$_2$, having a doping concentration of 2%, exhibits the highest catalytic activity against methylene blue (MB) in neutral, acidic, and alkaline solutions, as well as substantial inhibitory activity for bacterial strains such as *Escherichia coli* (*E. coli*). In summary, the modified catalyst provides a pathway to design highly efficient catalysts for all pH range water treatment as well as good activity against microbes.

1. Introduction

Water is fundamental for maintaining and developing all living things.[1] However, the water bodies are contaminated by heavy metal ions, synthetic dyes, and other aromatic contaminants primarily originating from agricultural and industrial sectors.[2] Around one ten million different dyes are used in the production processes in a number of industries for a wide variety of products, including paper, plastic, leather, paint, and printing. Among these dyes, methylene blue (MB) is dreadful because around 10% to 15% is released directly into the environment, and the atmosphere causes dangerous diseases such as skin inflammation, liver disorders, and cancer.[3] In recent years, removing contaminants and dyes from the aquatic environment has become challenging for researchers.[4]

Traditional water treatment procedures such as ion exchange, adsorption, chlorination, aerobic treatment, and adsorption can be utilized to remove organic pollutants

M. Ikram, B. Ilyas, A. Shahzadi
Solar Cell Applications Research Lab
Department of Physics
Government College University Lahore
Lahore, Punjab 54000, Pakistan
E-mail: dr.muhammadikram@gcu.edu.pk

A. Haider
Department of Clinical Sciences
Faculty of Veterinary and Animal Sciences
Muhammad Nawaz Shareef University of Agriculture (MNSUAM)
Multan, Punjab 66000, Pakistan

J. Haider
Tianjin Institute of Industrial Biotechnology
Chinese Academy of Sciences
Tianjin 300308, China

A. Ul-Hamid
Center for Engineering Research
Research Institute
King Fahd University of Petroleum & Minerals
Dhahran 31261, Saudi Arabia

A. Shahzadi
Faculty of Pharmacy
The University of Lahore
Lahore 54000, Pakistan

S. Goumri-Said
Physics Department
Colleges of Science and General Studies
Alfaisal University
P.O. BOX 50927, Riyadh 11533, Saudi Arabia

from the water. Regrettably, these techniques have several problems, including insufficient removal, significant energy use, and dye transfer.[5] In addition to the aforementioned methods, catalytic dye degradation in the existence of nanomaterials has attracted a great deal of attention from researchers due to its low affordability, minimal toxicity, high chemical stability, and ecologically benign qualities.[6] Nanomaterials were studied for their unique physicochemical properties and dye-degradation water treatment techniques.[7] Transition metal dichalcogenides have gained interest for their catalytic, electrical, and photocorrosion resistance,[8] making them ideal for specific applications like catalysis, lubricants, and energy storage and conversion. Among these nanomaterials, low dimensional materials like molybdenum disulfide (MoS_2) is a multilayer material that can be employed in a broad number of applications, including storage material,[9] catalysis,[10] and nanoelectronics.[11] MoS_2 possesses a direct bandgap energy (E_g) of 1.8 eV in two dimensions, while in one dimension, it possesses an indirect E_g of 1.2 eV.[12] In the layered structure of MoS_2, the atoms of molybdenum and sulfur are arranged in a hexagonal pattern, resulting in an S–Mo–S interaction.[11] MoS_2 with a layered structure has weak van der wall forces consisting of three stacked layers in which the molybdenum is sandwiched between two sulfur atoms (S–Mo–S).[13] Although MoS_2 has shown promising catalytic[14] and antimicrobial activities,[15,16] its applications are severely limited by lower reduction potential and poor stability in strongly acidic solutions, etc.[1,17] These attributes must be improved to maximize the application of MoS_2-based nanostructures in water treatment.

Here, we report the preparation of lanthanum (La)-doped MoS_2 nanosheets (NSs) to achieve a large number of active sites, tuned bandgap, and enhanced catalytic activity. Previously, rare-earth elements, such as Ce, Eu, and Gd, have been doped into MoS_2 to tune the electronic structure using their partially filled 4f and 5d orbitals.[18] Among these, lanthanum (La^{3+}) is a crucial activator in the photocatalysis of hydrogen evolution and serves as a facilitator for separating photogenerated electron–hole pairs.[19] La was found to strongly impact the structural, optical, and morphological characteristics of MoS_2 NSs. Interestingly, the modified NSs exhibited excellent activity and high stability in all pH range solutions and enhanced antimicrobial activity. We also performed first-principles calculations to examine the electronic structures of MoS_2 and the adsorption energies of MB on La-doped MoS_2 NS.

M. B. Kanoun
Department of Mathematics and Sciences
College of Humanities and Sciences
Prince Sultan
University
P.O. Box 66833, Riyadh 11586, Saudi Arabia

W. Nabgan
Departament d'Enginyeria Química
Universitat Rovira i Virgili
Tarragona 43007, Spain
E-mail: walid.nabgan@urv.cat

A. Mahmood
Center for Clean Energy Technology
School of Mathematical and Physical Sciences
Faculty of Science
University of Technology Sydney
Sydney 2007, Australia
E-mail: asif.mahmood@uts.edu.au

2. Experimental Section

2.1. Chemicals

Sodium molybdate dehydrates ($Na_2MoO_4 \cdot 2H_2O$, 99%), thiourea (N_2H_4CS), lanthanum nitrate hexahydrate ($La(NO_3)_3 \cdot 6H_2O$) were acquired from Sigma Aldrich (Germany). Oxalic acid ($C_2H_2O_4$) was procured from Mark (Germany) and utilized without purification.

2.2. Synthesis of La-Doped MoS_2

MoS_2 was synthesized hydrothermally; initially, 0.5 M colloidal solution of sodium molybdate dehydrates was prepared and added thiourea liquefied (1:1.5), respectively. pH 12 was adjusted using oxalic acid. Then, various concentrations of La (2%, 4%) were added, and the mixture was magnetically agitated for 45 min. Eventually, the solution was transferred to an autoclave to accomplish the reaction at 180 °C for 24 h and permitted to cool down at ambient temperature. After this, the obtained precipitate was centrifuged twice at 7500 rpm and sonicated for 5 h to attain a 2D layer. To obtain the resultant product, the solution was dried at 120 °C for 15 h (**Figure 1**).

2.3. Catalytic Activity (CA)

The CA of pristine and La-doped MoS_2 was determined against MB dye degradation. Initially, MB solutions were prepared at three pH values: acidic, neutral, and basic. Basic and acidic mediums were prepared using NaOH and H_2SO_4 solution. After this, 3 mL MB solution was mixed with 400 μL $NaBH_4$ solution, which acts as a reducing agent. Added 400 μL of catalyst into the solution, and MB color turned into leucomethylene blue, indicating the successful degradation of synthetic dye. The experiment was conducted at room temperature and examined the dye degradation using a UV–vis spectrophotometer. The degradation percentage was calculated using Equation (1)

$$\% \text{ Degradation} = (C_o - C_t / C_o) \times 100 \qquad (1)$$

Where C_o indicates dye concentrations at the initial time and C_t represents the dye concentrations at a specific time.
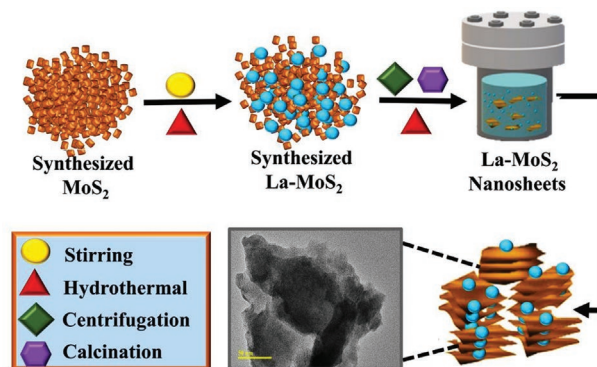

Figure 1. Synthesis diagram of La-doped MoS_2 Nanosheets.

2.4. Catalytic Mechanism

In the catalysis mechanism, two aspects are thought to be crucial: first, introducing a reducing agent and, second, incorporating a nanocatalyst into the dye. Generally, a reductant is a chemical substance that typically provides an electron to MB, acting as an oxidant. During the catalysis process, a redox reaction typically involves the transfer of an electron from a reductant to an oxidizing agent, leading to synthetic dye degradation. The degradation process in the absence of a nanocatalyst is slow and time-intensive. The inclusion of a catalyst increased degradation as the catalyst reduced the activation energy and enabled electron transfer from the BH_4^- (donor) to the MB^+ (acceptor). This research evaluated dye degradation by catalytic activity utilizing a reducing agent and a synthesized nanocatalyst.[20]

2.5. Isolation and Identification of MDR *Escherichia coli*

Raw milk samples were obtained by directly milking chosen lactating cows into sterile glassware and collecting them from various markets, veterinary hospitals, and farms located around the province of Punjab in Pakistan. Raw milk was brought into the laboratory at a temperature of 4 °C. MacConkey agar was utilized to count the number of coliforms in raw milk. Every plate was kept in an incubator for 48 h at 37 °C. In order to make a preliminary diagnosis of *E. coli*, colonial morphology was examined using Gram stain, and a number of other biochemical assays were performed with reference to Bergey's Manual of Determinative Bacteriology.[21]

2.5.1. Antibiotic Susceptibility

On Mueller Hinton agar (MHA), the antibiotic susceptibility test was carried out with the disc diffusion method developed by Bauer et al.[22] The experiment was carried out to assess the resistance of *E. coli* against ciprofloxacin (Cip) 5 µg antibiotic.[23] The turbidity of the *E. coli* cultures grown after purifying was adjusted to 0.5 MacFarland. After that, it was spread out on MHA (Oxoid Limited, Basingstoke, UK), and antibiotic discs were placed on the surface of the inoculation plate at a distance from one another to prevent the inhibition zones from collapsing into one another. After 24 h of incubation at 37 °C, the data were analyzed following the guidelines established by the Clinical and Laboratory Standard Institute.[24] The presence of a bacterium that is resistant to at least three antibiotics is required for it to be classified as MDR.[25]

2.5.2. Antimicrobial Activity

The inhibition zones against MDR *E. coli* have been measured using the agar well diffusion method to determine the in vitro antibacterial action potential of MoS_2 and La (2% and 4%) doped MoS_2. MacConkey agar plates have been inoculated with MDR *E. coli* at a concentration of 1.5×10^8 CFU mL^{-1} (0.5 McFarland standard). Pathogens of *E. coli* have always been successfully recovered from ovine mastitis fluid to evaluate the bactericidal efficacy of both pristine and doped nanostructures. Infectious bacterial treatments have been scraped on agar plates, and sterile cork borers have been used to create holes with a diameter of 6 mm each. A positive control was provided by the common medication ciprofloxacin (5 µg/50 mL), and negative control was supplied by dilute iodine water (50 µL). The boreholes have been filled with host and varied concentration levels of the doped nanostructure at high and low concentrations (1.0 mg/50 µL and 1.0 mg/50 µL, respectively). After that, the plates were let to sit in an incubator at room temperature for one whole day, and the inhibited zones surrounding the wells were measured using a Vernier caliper. After the diameters (in millimeters) of the inhibition zones that encircled the wells had been measured, the antibacterial activity of the samples that had been generated could be assessed.[26]

2.5.3. Statistical Analysis

The zones of inhibition measurement size (mm) were used to determine the antimicrobial effectiveness, and the diameters of the inhibition zones were statistically analyzed using one-way analysis of variance (ANOVA) in SPSS 20.[27]

3. Results and Discussion

XRD was utilized to assess the structural characteristics, phase purity, and layer spacing of the synthesized samples, see **Figure 2**a. The diffraction pattern of MoS_2 at 14.37°, 32.67°, and 33.50° is indexed to the planes (002), (100), and (101), indicating the hexagonal crystal structure and are well matched with standard data (00-037-1492).[28] The monoclinic phase exhibited by Mo_2S_3 at 23.12°, 34.55°, 45.80°, and 53.41° referred to planes as ($\overline{1}$02), (111), (104), and ($\overline{3}$11), corresponds to card no. (03-065-0445).[29] The diffraction peak at 19.23° is ascribed to the plane (110) with (JCPDS card no. 01-082-1709) demonstrating rhombohedral crystal structure of Mo_3S_4. The peak intensity reduced slightly in La-doped (2%) and pure (4%) MoS_2 samples, showing lower crystallinity after La doping.[19] After doping, a slight shift in peaks was observed, attributed to lanthanum (La^{3+}) higher ionic radius compared to molybdenum (Mo^{4+}).[30] The connection of functional groups to various vibrational modes was assessed using FTIR spectroscopy between 4000 and 500 cm^{-1} (Figure 2b). The band observed at 3371 cm^{-1} assigned to the bending mode of O–H attributed to water molecules. S–S and S–O stretching appeared at bands 840 and 1124 cm^{-1}, respectively.[30] The bands found around 1415 and 1611 cm^{-1} are linked to sulfur production coupled with active MoS_2 sites and extended C–H band.[31] MoS_2 was found to have a band at 480 cm^{-1}, assigned to the Mo–S bonding.[32] Characteristic bands around 1380, 931, and 2170 cm^{-1} alluded to Mo–O, S–S bond, and N=C transmittance, respectively.[11,33] Furthermore, bright circular rings were explored by the SAED patterns, suggesting the polycrystalline nature of prepared samples. The obtained results are correlated with XRD patterns (see **Figure 3**c–e).

UV–vis spectrophotometer was used to examine absorption spectra and bandgap energy of dopant-free and La-doped
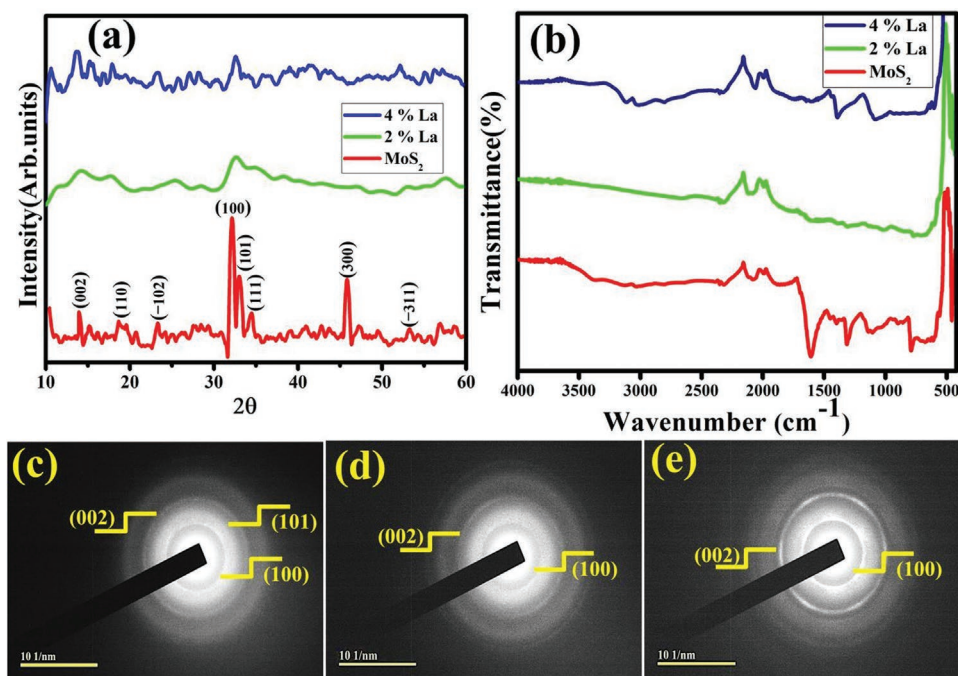
Figure 2. a) X-ray diffraction patterns, b) FTIR spectra, and c–e) SAED profiles of as-prepared and La-doped (2 %, 4 %) MoS$_2$ nanosheets.

MoS$_2$ nanosheets (Figure 3a,b). The characteristic absorption spectra displayed at $\lambda_{max} = 320$ were assigned to the excitonic characteristics of MoS$_2$.[34] A redshift is observed with the La doping as the absorption band extends to higher wavelengths. Tauc's plot was used to compute the optical bandgap energies (3.87–3.47 eV) of samples. To study the process of electron–hole
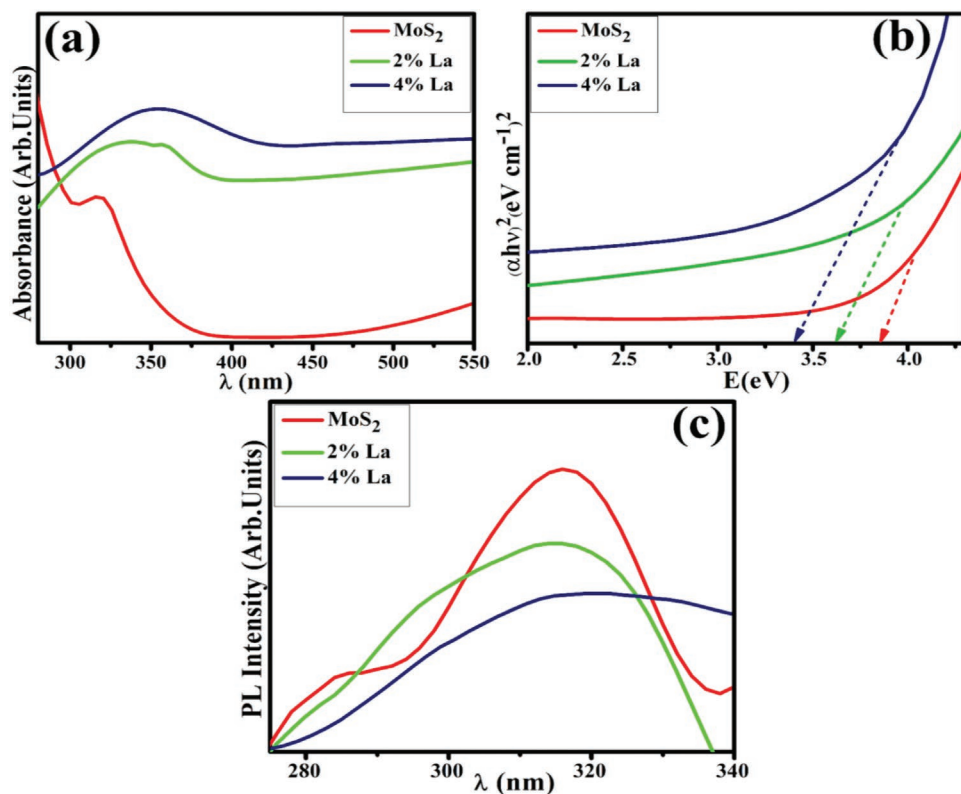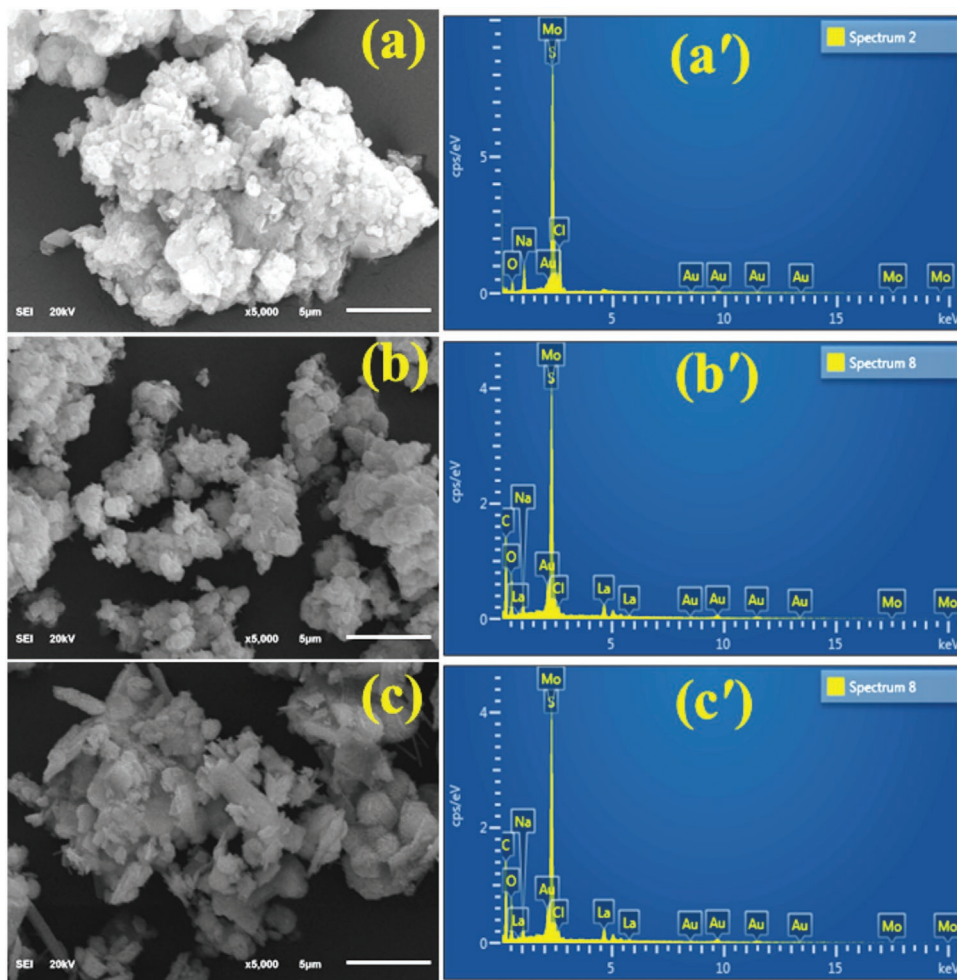

Figure 3. a) Optical spectra of doped NS, b) bandgap energy plot, c) PL spectra of MoS$_2$ and La-doped (2 %, 4 %) MoS$_2$ NSs.

pair recombination in MoS$_2$ and La-doped MoS$_2$ samples, PL spectroscopy was employed (Figure 3c). Because of the strong association between the PL effect of 2D MoS$_2$ and its electronic-band structure, this technique provides an efficient way to characterize the material.[35] The PL spectra seemed to have the highest intensity, ≈320 nm, which was comparable with the UV–vis spectra[34a] Observed high excitation wavelength corresponds to surface states, quantum confinement phenomenon, and edge sites of MoS$_2$ NSs.[36] According to findings, PL intensity gradually decreased upon the desired incorporation of La. The reduction in PL intensity for 4% La-MoS$_2$ is attributed to effective charge transfer due to the optimum doping ratio.[19]
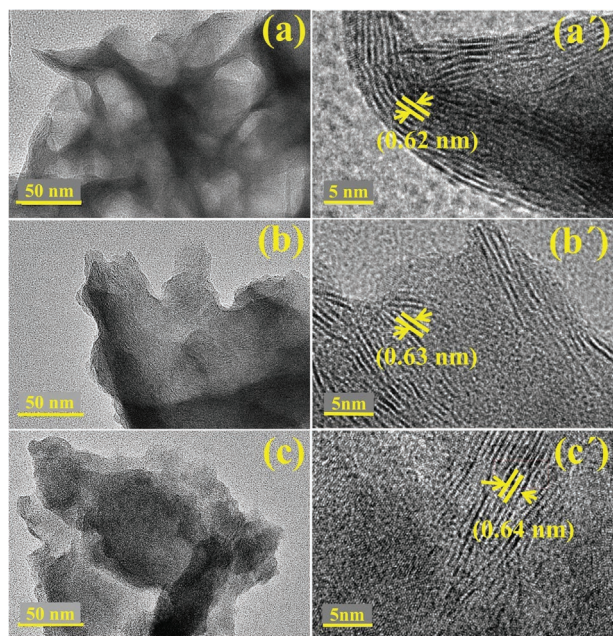
FESEM was employed to confirm the surface morphological study of produced La-doped MoS$_2$, as depicted in **Figure 4**a–c. It can be seen that the particles had a spherical shape and a high porosity which raids. The porosity between aggregated particles assists in the rapid decomposition of organic dyes (Figure 4a). The introduction of La in low amounts leads to the formation of nanoclusters, which, in turn, triggers agglomeration and the beginning of rod development (Figure 4b). Moreover, a few rod-shaped particles were detected with increasing doping concentration of La (Figure 4c). To assess the confirmation of synthesized pristine and the presence of dopants in MoS$_2$, the

EDS technique was employed (Figure 4a′–c′). The excellent purity of MoS$_2$ is validated by the prominent peaks of Mo and S, whereas the peak of C is most likely attributed to carbon tape in the sample mounting process. In Figure 4b′,c′, the 4.6% presence of La confirmed the successful doping of lanthanum in doped MoS$_2$. Sodium (Na) peaks in spectra originate from using NaOH to control pH during NSs synthesis, while the coating induces Au peaks sputtered on the specimens to prevent charging effects.

The morphological feature of dopant-free and doped MoS$_2$ was investigated by employing TEM images, as displayed in **Figure 5**a–c. The TEM analysis in Figure 5a exhibit that this might be a porous structure formed by hierarchical aggregation of 2D MoS$_2$ sheets that will improve the surface area. Obtained nanosheets were overlayered by the introduction La, where the shadowed portion of the images explores the multilayer nanosheet structure of MoS$_2$, causing the particle structure to become asymmetrical (see Figure 5b,c). Furthermore, the estimated d-spacing value of produced nanosheets was computed as 0.62 nm for dopant-free samples and fulfills the theoretical d-spacing of the MoS$_2$ crystallographic plane (002) while interlayer spacing for doped samples were 0.62–0.64 nm, as shown in Figure 5a′–c′), these measurements corresponded
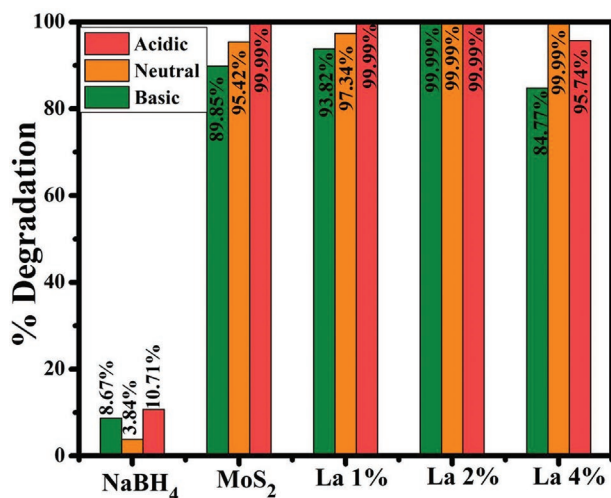

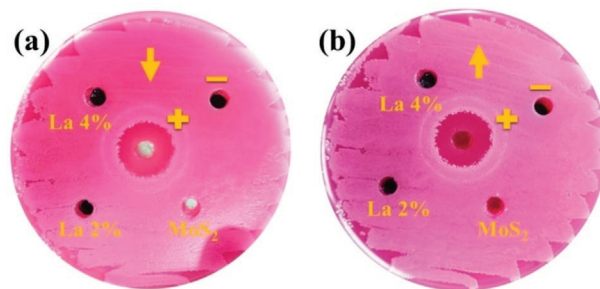**Figure 4.** a–c) SEM and a′–c′) EDS analysis of MoS$_2$ and La-doped MoS$_2$.

**ADVANCED
SCIENCE NEWS**

www.advancedsciencenews.com

**ADVANCED
MATERIALS
INTERFACES**

www.advmatinterfaces.de

Figure 5. a–c) TEM and a′–c′) HR-TEM micrographs of as-prepared and La (2% and 4%)-doped MoS$_2$ NSs.

Figure 7. Antibacterial activity of prepared nanostructures against *E. coli* a) low dose, b) high dose.

extremely well with the XRD findings (Figure 2a). The minor shift in interlayer spacing from 0.62 to 0.64 nm with La doping indicates that the lattice has not changed considerably upon doping. There is no change in lattice upon doping, as proved by the (002) plane in all three samples.

Catalytic activity was accessed by degradation of MB with NaBH$_4$ in the presence of prepared nanocatalyst in basic (pH = 12), neutral (pH = 7), and acidic (pH = 4) mediums, **Figure 6**. Degradation without catalyst was maximum of 10.71% in 10 min. With the addition of a catalyst, the calculated % degradation was 89.85%, 93.82%, 99.99%, 84.77% in basic medium, 95.42%, 97.34%, 99.99%, 99.99% in neutral medium, and 99.99%, 99.99%, 99.99%, 95.74% in an acidic medium for MoS$_2$

and La-doped MoS$_2$ (1%, 2%, and 4%), respectively. MoS$_2$ doped with 2% La showed the highest degradation, possibly attributed to exceptional adsorption performance due to important parameters, including surface area, interfacial sites, and pore width, indicating 2% is optimal lanthanum doping. As the concentration increased to 4%, the degradation of MB decreased in an acidic medium.[37] The increasing dopant concentration might partially block the active sites of MoS$_2$, resulting in a decrease in catalytic activity.[38]

The suitable diffusion method was used to test the bactericidal effectiveness of La-doped MoS$_2$ concerning the *E. coli* pathogen (see **Figure 7**). At both the lowest and highest doses, significant ($p < 0.05$) inhibition zones were found at 0.9–2.05 mm and 1.30–2.05 mm, respectively (**Table 1**). Comparative analyses of the inhibition zones for *E. coli* were carried out using a negative control consisting of DI water (0 mm) and a positive control consisting of ciprofloxacin (5 mm), respectively. In point of fact, the antibacterial activity of the nanostructures can be attributed to a variety of phenomena, such as electrostatic contact or interactions with OH$^-$ and H$_2$O present at the surface. These interactions both result in the production of reactive oxygen species (ROS), which are responsible for the nanostructures' antibacterial properties. Additionally, the dimensions, shapes, and mass-to-surface ratios of prepared doped NPs depend on oxidative stress. This is because tiny particles instantly discharge ROS, which degrades the cytoplasmic constituents of bacteria, ultimately leading to the collapse of the bacteria.[39] Antibacterial activities were shown to be significantly improved due to the higher concentration of NPs that resulted from contact. Because both metallic species coexist in the NPs, a synergistic effect is formed, which results in a significant increase in the antibacterial activity of the doped NPs.[40] Another way nanoparticles interact with germs is by vigorous

Figure 6. Percentage degradation of MB using nanocatalyst at different pH

Table 1. Antibacterial activity of La-doped MoS$_2$ nanostructures.

| Samples	Inhibition zones [mm]	
	0.5 mg/50 μL	1.0 mg/50 μL
MoS$_2$	0.9	1.30
La 2%	1.45	1.80
La 4%	2.05	2.05
Ciprofloxacin	5	5
DIW	0	0
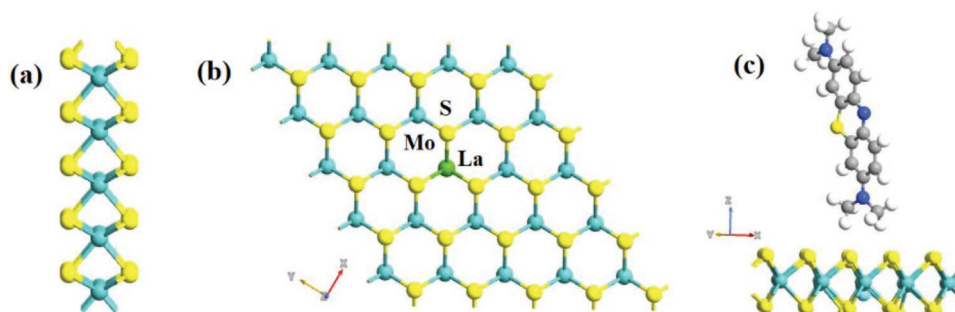
Figure 8. a) Side view, b) Top view of La-doped MoS_2, and c) and side view of the adsorption of MB on the MoS_2 monolayer.

cationic interaction with negatively charged microbial components, which ultimately disintegrates bacteria.[26,41]

To explore the electronic properties of the pristine and La-doped MoS_2 NS, the linear combination of atomic orbital (LCAO) basis sets were employed with the PseudoDojo pseudopotential,[42] as implemented in the QuantumATK package.[43] Within the generalized gradient approximation (GGA), the Perdew–Burke–Ernzerhof (PBE)[44] functional and DFT-1/2 approach[45] were used to characterize the exchange and correlation effects. When the atomic force reached 0.05 eV Å^{-1}, and the highest energy variation between the two stages was less than 10^5 eV, the structure was optimized. The cutoff for density mesh of 10^5 Ha was employed, and the $4 \times 4 \times 1$ set of k-points was chosen for the structure optimization and the $6 \times 6 \times 1$ set for electronic property calculations. A $5 \times 5 \times 1$ supercell based on a hexagonal unit cell was adopted to model the MoS_2 monolayer, and a vacuum space of 15 Å was employed on the z-axis to avoid artificial interaction between nearby layers,[33] as shown in **Figure 8**a. The La-doped MoS_2 monolayer is modeled by substituting one Mo atom with one La atom, yielding a doping concentration of 4%, as displayed in Figure 7b. The lattice constant of the optimized structure MoS_2 monolayer is found to be $a = b = 3.25$ Å, which is consistent with the reported investigations,[6,7] and the bond length of Mo–S and S–S is defined to be 2.48 and 3.23 Å, respectively.[46] The spin–orbit coupling (SOC) and noncollinear mode are considered in calculating the electronic structures.

To further get the stability of La doping into MoS_2 monolayers, the binding energy is computed as follows,[47] $E_b = E_{\text{doped Mos2}} - E_V - E_{La}$, where $E_{\text{doped Mos2}}$ stands the total energy of the La-doped monolayer. E_V and E_{La} are the total energies of MoS_2 with vacancies and isolated La atoms, respectively. The binding energy with the equilibrium distance is -10.4 eV, which relates to the most significant binding effect. To describe materials based on their electronic properties, the electronic band structure and the density of states of the pure and La-doped MoS_2 monolayer are calculated using the DFT-1/2 method with SOC contribution, as displayed in **Figure 9**. From the analysis of the results, the bandgap of monolayer MoS_2 is found to be 1.93 eV, which is consistent with the experimental measurement (1.90 eV) and previous theoretical values.[46] Furthermore, the top valence bands and the bottom conduction bands of the pure monolayer MoS_2 are primarily made up of the states Mo 4d and S 3p. The doping of the La atom changes the electronic character of the system, which can introduce the new states within the bandgap region, allowing for further energy transitions to be induced. It is observed that the in-gap states reveal strong hybridization with Mo 5d and S 3p states that are around the dopant with a small contribution from La 5d states. The calculations reveal that a small total magnetic moment of 0.833 μ$_B$ is induced in doping material. The adsorption energy (E_{ads}) of the MB molecule on the pristine and La-doped monolayer MoS_2 is expressed[48] as; $E_{ads} = E_{MoS2 - MB} - E_{MoS2} - E_{MB}$,
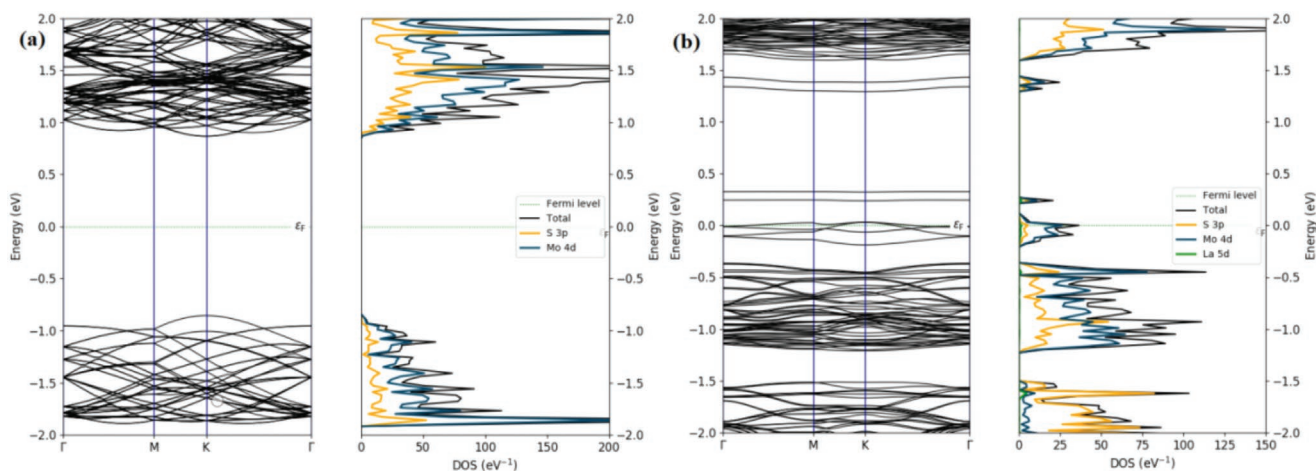
Figure 9. Calculated Band structures and DOS of a) pristine and b) La-doped monolayer MoS_2

© 2023 The Authors. Advanced Materials Interfaces published by Wiley-VCH GmbH

where $E_{MoS_2 - MB}$ denotes the total energy of the La-doped MoS_2 monolayer with an MB, $E_{monolayer}$ represents the total energy of undoped and La-doped MoS_2 lattice, and E_{MB} is the energy of a MB molecule. The estimated E_{ads} values are found to be −0.225 and −0.954 eV for the pristine and La-doped monolayer MoS_2, respectively. Negative adsorption energy can cause the MB to adsorb on pure and La-doped MoS_2 nanosheets with more excellent stability.

4. Conclusion

The current work is based on the preparation of La-doped MoS_2 NSs via hydrothermal technique. XRD spectra of MoS_2 and La-doped MoS_2 NSs unveiled multiple crystal structures, including (hexagonal, monoclinic, and rhombohedral) and upon La doping, peak intensity decreased gradually. The functional group and the band at 480 cm^{-1} confirmed Mo–S bond existence in a pure sample confirmed by FTIR. The reduction in bandgap energy from 3.87 to 3.47 eV with La doping was revealed extracted from absorption spectra obtained through UV–vis spectrophotometer. The elemental composition was explored by EDS analysis, where Mo and S peaks represent the formation of pure sample and La peaks for doped MoS_2 NSs. The first principles methods show that La doping changes the electronic character of the pristine monolayer, which can introduce the new states within the bandgap region, allowing for further energy transitions to be induced. Moreover, the adsorption energies of the MB on La-doped MoS_2 nanosheets were examined, and stable structures were found. La (2%) doped MoS_2 exhibited maximum CA against MB degradation in an acidic and neutral medium of about 99.99%. The substantial inhibitory zones for *E. coli* were detected following the addition of La to MoS_2. According to the findings of this work, the synthesized MoS_2 and La-doped NSs have shown to be composite innovations with excellent catalytic efficacy for cleaning industrially contaminated water. These materials have the potential to be put to use in applications in biomedicine that are not very costly.

Conflict of Interest

The authors declare no conflict of interest.

Data Availability Statement

The data that support the findings of this study are available from the corresponding author upon reasonable request.

[1] S. Chen, L.-W. Wang, *Chem. Mater.* **2012**, *24*, 3659.

[2] S. Dervin, D. D. Dionysiou, S. C. Pillai, *Nanoscale* **2016**, *8*, 15115.

[3] M. Junaid, M. Imran, M. Ikram, M. Naz, M. Aqeel, H. Afzal, H. Majeed, S. Ali, *Appl. Nanosci.* **2019**, *9*, 1593.

[4] K. Naseem, Z. H. Farooqi, R. Begum, W. Wu, A. Irfan, A. G. Al-Sehemi, *Macromol. Chem. Phys.* **2018**, *219*, 1800211.

[5] a) H. Eccles, *Recent Trends Biotechnol., Proc. Ninth Natl. Conv. Chem. Eng. Int. Symp.* **1999**, *17*, 462; b) I. Saha, S. Bhattacharya, A. Mukhopadhyay, D. Chattopadhyay, U. Ghosh, D. Chatterjee, *Int. J. Chem. Sci. Technol.* **2013**, *3*, 59.

[6] M. Ali, S. Sharif, S. Anjum, M. Imran, M. Ikram, M. Naz, S. Ali, *Mater. Res. Exp.* **2020**, *6*, 1250d1255.

[7] A. Bari, M. Ikram, A. Haider, A. Ul-Hamid, J. Haider, I. Shahzadi, G. Nazir, A. Shahzadi, M. Imran, A. Ghaffar, *Nanoscale Adv.* **2022**, *4*, 2713.

[8] M. Velický, P. S. Toth, *Appl. Mater. Today* **2017**, *8*, 68.

[9] Y. Li, H. Wang, L. Xie, Y. Liang, G. Hong, H. Dai, *J. Am. Chem. Soc.* **2011**, *133*, 7296.

[10] J. Chen, N. Kuriyama, H. Yuan, H. T. Takeshita, T. Sakai, *J. Am. Chem. Soc.* **2001**, *123*, 11813.

[11] K. Lalithambika, K. Shanmugapriya, S. Sriram, *Appl. Phys. A* **2019**, *125*, 1.

[12] a) J. Ryou, Y.-S. Kim, S. Kc, K. Cho, *Sci. Rep.* **2016**, *6*, 1; b) X. Li, H. Zhu, *J. Mater.* **2015**, *1*, 33.

[13] P. Chen, X. Liu, R. Jin, W. Nie, Y. Zhou, *Carbohydr. Polym.* **2017**, *167*, 36.

[14] Y. Zhang, W. Xiu, S. Gan, J. Shan, S. Ren, L. Yuwen, L. Weng, Z. Teng, L. Wang, *Front. Bioeng. Biotechnol.* **2019**, *7*, 218.

[15] M. Santosham, A. Chandran, S. Fitzwater, C. Fischer-Walker, A. H. Baqui, R. Black, *Lancet* **2010**, *376*, 63.

[16] G. Solomon, R. Mazzaro, V. Morandi, I. Concina, A. Vomiero, *Crystals* **2020**, *10*, 1040.

[17] Q. Ding, B. Song, P. Xu, S. Jin, *Chem* **2016**, *1*, 699.

[18] a) T. Lei, S. Wu, Y. Zhang, H. Guo, D. Chen, Z. Zhang, *Acta Phys. Sin.* **2014**, *63*, 067301; b) B. Qu, Y. Sun, L. Liu, C. Li, C. Yu, X. Zhang, Y. Chen, *Sci. Rep.* **2017**, *7*, 42772.

[19] K. Nadeem Riaz, N. Yousaf, M. Bilal Tahir, Z. Israr, T. Iqbal, *Int. J. Energy Res.* **2019**, *43*, 491.

[20] a) U. Qumar, M. Ikram, M. Imran, A. Haider, A. Ul-Hamid, J. Haider, K. Riaz, S. Ali, *Dalt. Trans.* **2020**, *49*, 5362; b) J. R. Ludwig, C. S. Schindler, *Chem* **2017**, *2*, 313.

[21] J. G. Holt, N. R. Krieg, P. H. Sneath, J. T. Staley, S. T. Williams, Genus Salmonella, Bergey's manual of determinative bacteriology, **1994**, pp. 175–289.

[22] A. Bauer, W. Kirby, J. Sherris, M. Turck, *Am. J. Clin. Pathol.* **1966**, *493*, 496.

[23] F. Adzitey, R. Yussif, R. Ayamga, S. Zuberu, F. Addy, G. Adu-Bonsu, N. Huda, R. Kobun, *Microorganisms* **2022**, *10*, 1335.

[24] N. Bakker, M. Dubbeling, S. Guendel, U. Sabel-Koschella, H. d. Zeeuw, *Growing cities, growing food: urban agriculture on the policy agenda. A reader on urban agriculture*, Deutsche Stiftung fur Internationale Entwicklung (DSE), Feldafing, Germany **2000**.

[25] B. Iwalokun, A. Ogunledun, D. Ogbolu, S. Bamiro, J. Jimi-Omojola, *J. Med. Food* **2004**, *7*, 327.

**ADVANCED
SCIENCE NEWS**

www.advancedsciencenews.com

**ADVANCED
MATERIALS
INTERFACES**

www.advmatinterfaces.de

[26] A. Haider, M. Ijaz, M. Imran, M. Naz, H. Majeed, J. Khan, M. Ali, M. Ikram, *Appl. Nanosci.* **2020**, *10*, 1095.

[27] A. Haider, M. Ijaz, S. Ali, J. Haider, M. Imran, H. Majeed, I. Shahzadi, M. M. Ali, J. A. Khan, M. Ikram, *Nanoscale Res. Lett.* **2020**, *15*, 50.

[28] M. Mathankumar, K. Karthick, A. K. Nanda Kumar, S. Kundu, S. Balasubramanian, *ACS Sustainable Chem. Eng.* **2021**, *9*, 14744.

[29] T. C. Mangan, B. E. McCandless, K. D. Dobson, R. W. Birkmire, *J. Appl. Phys.* **2015**, *118*, 065303.

[30] M. K. Kumar, J. T. Kalathi, *J. Alloys Compd.* **2018**, *748*, 348.

[31] S. Krithika, J. Balavijayalakshmi, *Mater. Today: Proc.* **2022**, *50*, 17.

[32] S. Saha, N. Chaudhary, H. Mittal, G. Gupta, M. Khanuja, *Int. Nano Lett.* **2019**, *9*, 127.

[33] A. Raza, U. Qumar, A. Haider, S. Naz, J. Haider, A. Ul-Hamid, M. Ikram, S. Ali, S. Goumri-Said, M. B. Kanoun, *Dalton Trans.* **2021**, *50*, 6598.

[34] a) D.-H. Kim, C. Kim, D. Kim, S. Y. Lee, D.-J. Lee, H.-D. Kim, G. T. Kim, *Appl. Surf. Sci.* **2021**, *535*, 147661; b) V. Nguyen, Q. Dong, L. Yan, N. Zhao, P. H. Le, *J. Lumin.* **2019**, *214*, 116554.

[35] X. Gan, H. Zhao, X. Quan, *Biosens. Bioelectron.* **2017**, *89*, 56.

[36] H. Yu, J. Xu, H. Guo, Y. Li, Z. Liu, Z. Jin, *RSC Adv.* **2017**, *7*, 56417.

[37] a) H. Wang, H. Ye, X. Tang, Y. Wang, L. Zhao, *J. Environ. Chem. Eng.* **2022**, *10*, 107857; b) J. Nešić, D. D. Manojlović, I. Anđelković, B. P. Dojčinović, P. J. Vulić, J. Krstić, G. M. Roglić, *J. Mol. Catal. A: Chem.* **2013**, *378*, 67.

[38] R. Rahman, D. Samanta, A. Pathak, T. K. Nath, *RSC Adv.* **2021**, *11*, 1303.

[39] a) M. Hans, J. C. Támara, S. Mathews, B. Bax, A. Hegetschweiler, R. Kautenburger, M. Solioz, F. Mücklich, *Appl. Surf. Sci.* **2014**, *320*, 195; b) J. P. Ruparelia, A. K. Chatterjee, S. P. Duttagupta, S. Mukherji, *Acta Biomater.* **2008**, *4*, 707.

[40] W. Fang, C. Xu, J. Zheng, G. Chen, K. Jiang, *RSC Adv.* **2015**, *5*, 39612.

[41] A. Arshad, J. Iqbal, Q. Mansoor, *Nanoscale* **2017**, *9*, 16321.

[42] M. J. van Setten, M. Giantomassi, E. Bousquet, M. J. Verstraete, D. R. Hamann, X. Gonze, G.-M. Rignanese, *Comp. Phys. Commun.* **2018**, *226*, 39.

[43] S. Smidstrup, T. Markussen, P. Vancraeyveld, J. Wellendorff, J. Schneider, T. Gunst, B. Verstichel, D. Stradi, P. A. Khomyakov, U. G. Vej-Hansen, *J. Phys. Condens. Matter* **2019**, *32*, 015901.

[44] J. P. Perdew, K. Burke, M. Ernzerhof, *Phys. Rev. Lett.* **1996**, *77*, 3865.

[45] a) L. G. Ferreira, M. Marques, L. K. Teles, *AIP Adv.* **2011**, *1*, 032119; b) M. B. Kanoun, S. Goumri-Said, *Mater. Today Energy* **2021**, *21*, 100796.

[46] a) N. Lu, H. Guo, L. Li, J. Dai, L. Wang, W.-N. Mei, X. Wu, X. C. Zeng, *Nanoscale* **2014**, *6*, 2879; b) A. Splendiani, L. Sun, Y. Zhang, T. Li, J. Kim, C.-Y. Chim, G. Galli, F. Wang, *Nano Lett.* **2010**, *10*, 1271.

[47] M. B. Kanoun, *J. Alloys Compd.* **2018**, *748*, 938.

[48] J. Hassan, S. Naz, A. Haider, A. Raza, A. Ul-Hamid, U. Qumar, J. Haider, S. Goumri-Said, M. B. Kanoun, M. Ikram, *Mater. Sci. Eng., B* **2021**, *272*, 115365.

2202404 (9 of 9)